Strong Paramagnetism of Gold Nanoparticles Deposited on a *Sulfolobus acidocaldarius S* Layer

J. Bartolomé,[1,2,*] F. Bartolomé,[1,2] L. M. García,[1,2] A. I. Figueroa,[1,2] A. Repollés,[1,2] M. J. Martínez-Pérez,[1,2] F. Luis,[1,2]
C. Magén,[2,3] S. Selenska-Pobell,[4] F. Pobell,[4] T. Reitz,[4] R. Schönemann,[4] T. Herrmannsdörfer,[4] M. Merroun,[5]
A. Geissler,[4] F. Wilhelm,[6] and A. Rogalev[6]

[1]*Instituto de Ciencia de Materiales de Aragón (ICMA), CSIC—Universidad de Zaragoza, E-50009 Zaragoza, Spain*
[2]*Departamento de Física de la Materia Condensada, Universidad de Zaragoza, E-50009 Zaragoza, Spain*
[3]*Laboratorio de Microscopías Avanzadas (LMA), Instituto de Nanociencia de Aragón (INA)—ARAID,
Universidad de Zaragoza, E-50018 Zaragoza, Spain*
[4]*Institute of Resource Ecology and Dresden High Magnetic Field Laboratory, Helmholtz-Zentrum Dresden-Rossendorf,
D-01328 Dresden, Germany*
[5]*Department of Microbiology, University of Granada, E-18071 Granada, Spain*
[6]*European Synchrotron Radiation Facility (ESRF)- BP 220, F-38043 Grenoble, France*
(Received 28 June 2012; published 10 December 2012)

Magnetic properties of Au nanoparticles deposited on an archaeal *S* layer are reported. X-ray magnetic circular dichroism and superconducting quantum interference device magnetometries demonstrate that the particles are strongly paramagnetic, without any indication of magnetic blocking down to 16 mK. The average magnetic moment per particle is $M_{\text{part}} = 2.36(7)\ \mu_B$. This contribution originates at the particle's Au 5*d* band, in which an increased number of holes with respect to the bulk value is observed. The magnetic moment per Au atom is 25 times larger than any measured in other Au nanoparticles or any other configurations up to date.

Gold nanoparticles (NPs) are being actively investigated because of their importance for medicine as antitumoral or antirheumatic vectors, on one hand, and, on the other hand, because of the fascinating size effects that their optical and, more recently, magnetic properties show under special conditions [1,2]. Thiol functionalized templates [3] can be used to promote the growth of Au NPs in organized arrays and to enhance the surface to volume ratio of atoms in the NP. We have previously shown that Au NPs could be successfully grown onto the naturally thiol-containing proteinatious surface layer (*S* layer) of *Sulfolobus acidocaldarius* without any chemical functionalization by thiol groups [4]. Au may acquire a magnetic moment both extrinsically, through polarization by a neighboring magnetic material, as in Au-capped Co particles [5] and Au-covered thin Co films [6], or by alloying with other metals such as Fe [7], and intrinsically, as observed in Au films capped with thiol groups [8], NPs sheathed by polyallyl amine hydrochloride [9], thiol bonds [10], or even bare NPs [11]. In bulk gold, a Pauli paramagnetic magnetization has been recently evidenced [12]. In many of these cases, the magnetic moment of Au has been determined from measurements of the overall sample magnetization, performed with superconducting quantum interference device (SQUID) magnetometers [1,8,10,11]. However, only an element-selective technique, such as x-ray magnetic circular dichroism (XMCD) measured at the Au $L_{2,3}$ edges, is able to guarantee that effectively Au is at the origin of the observed magnetic moments [4–7,9,12–14].

In this Letter we report the results of XMCD measurements performed at the Au $L_{2,3}$ edges that show the existence of an intrinsic magnetic moment per Au atom that is at least 25 times larger than any other previously found. From the temperature dependence of the XMCD we find that the NPs magnetic behavior is paramagnetic and, from very low temperature microSQUID measurements, that this behavior is maintained down to 16 mK, i.e., that no superparamagnetic blocking occurs in this case.

The biological matrix used for the Au NPs fabrication consists of empty microbial cells ("ghosts"), composed only of the extremely stable, highly ordered and porous proteinaceous *S* layer of the thermoacidophilic archaeon *Sulfolobus acidocaldarius*, which has a *p*3 symmetry [15]. The monomers of this *S* layer contain two cysteine amino acid residues with a C-S-H thiol chain each. Three of these monomers surround each pore, which render the *S* layer membrane permeable. Hence, 6 sulphur atoms are available per pore. At some of these pore sites, the Au starts to nucleate randomly. *S* atoms are also present in the ghost *S* layer as sulfonyl groups. They probably play no role in the formation of the Au particles since they cannot reduce metals. However, in their proximity there is a high number of glutamate and lysine stretches supplying carboxylic or amino and hydroxylic groups that may take part in the initial nucleation of Au(III). After chemical reduction with dimethylaminoboran hydride, the deposited Au(III) transforms into Au(0) NPs on the *S* layer. The samples obtained by this method are flat scales of a few tenths of mm side and a few microns thick. Further details on the sample preparation are given in Ref. [4]. A collection of scales obtained in different batches, amounting to 15 mg, were used in this work.

Nanoparticles were dispersed by sonication on a Cu TEM grid and observed by transmission electron microscopy (TEM) in a high resolution Philips CM 200 transmission electron microscope at an acceleration voltage of 200 kV, and high-angle annular dark-field scanning transmission electron microscopy (HAADF-STEM) in a probe corrected FEI Titan operated at 300 kV. These experiments show the existence of three types of particles [Figs. 1(a) to 1(c)]: crystalline nanoparticles with average diameters in the range 4–5 nm [see Fig. 1(b)], Au clusters with no crystalline ordering and an average diameter below 2 nm [Fig. 1(c)], and numerous single Au atoms dispersed on the grid [see Fig. 1(c)]. Besides, bright-field TEM images were analyzed to determine the particle distribution at a statistical level [see histogram in Fig. 1(a)] yielding an average particle size $\langle D \rangle = 2.6(1)$ nm.

The x-ray absorption experiments were performed at the ID12 beam line of the European Synchrotron Radiation Facility. Incoming radiation was monochromatized by a double-Si(111) crystal with a polarization rate over 95% in all cases. The detection technique was total fluorescence yield in backscattering geometry. X-ray absorption near edge structure (XANES) was measured at the Au $L_{2,3}$ and sulphur K edges. The presence of Au-S bonds was studied by comparison of the sulphur K-edge XAS spectra ($1s \rightarrow 3p$ transition) measured on the Au NPs sample with those of a Au-free S-layer sample. For reference, the L-cysteine was also measured. The sample supporting the Au NPs shows a distinct line on the sulphur XANES at $E = 2476.1$ eV, which is absent from spectra recorded on the Au-free sample (see peak 4 in Fig. 2). This extra line has been associated with the presence of S-Au bonds [16,17].

To obtain a quantitative determination of the average number of holes in the Au 5d band, n_h, the contribution from transitions to the continuum has to be subtracted from the experimental Au $L_{2,3}$ XAS intensity. This subtraction allows us to obtain the white line integrated intensities, I_{L2} and I_{L3} and its sum $r^* = I_{L2} + I_{L3}$, which is the relevant parameter.

Since the intensities of the white lines are very small, instead of subtracting an analytical step function, as it is customary in simpler cases, the Au foil XANES white line is taken as reference [Fig. 3(a)]. It is observed that the Fermi energy of the Au NPs shifts by $\Delta E_0 \approx 1$ eV with respect to the bulk value. The area differences for Au spectra have been integrated between $E - E_0 = -25$ eV, where E_0 is the energy at the inflection point of the XAS peak low-energy tail, and $E - E_0 = 25$ eV, where the white lines of the Au foil and S-layer Au NP coalesce. Once the $r^* = 1.14(8)$ eV area has been determined, the number of holes can be calculated as $n_h = n_h^{\text{Au-foil}} + \Delta n_h$. Here, $n_h^{\text{Au-foil}} = 0.617$ holes [18,19] and $\Delta n_h = r^*/C = 0.152(8)$, with $C = 7.845$ holes/eV determined from the scaling factor deduced experimentally for a Au_4Mn alloy [19]. It then follows that $n_h = 0.769(8)$ holes. The comparison with the bulk value indicates that, on average, there is a noticeable transfer of electrons from the Au 5d band towards the atoms surrounding the Au NP.

The XMCD signal was obtained by the difference of two XANES spectra, recorded with opposite helicities at $H = \pm 170$ kOe parallel to the beam direction. Figure 3(b) shows an XMCD spectrum measured on the Au:S-layer NP samples at the Au $L_{2,3}$ edges, for $T = 2.7$ K and $H = 170$ kOe. The dominant signal corresponds to $2p \rightarrow 5d$ transitions since the contributions due to the dipolar ($2p \rightarrow 6s$) and quadrupolar ($2p \rightarrow 6p$) are negligible. Therefore, the XMCD yields information on the magnetic moment per Au atom arising, almost exclusively, from the 5d states [19]. Sum rules [20] allow us to obtain
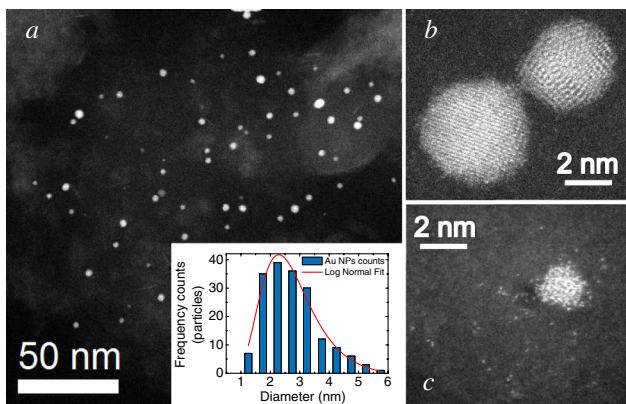

FIG. 1 (color online). HAADF-STEM images of Au NPs dispersed on a TEM Cu grid after sonication. (a) Low magnification image of Au NPs along with the histogram of the diameter distribution (inset). The solid line is a log-normal distribution with $\langle D \rangle = 2.6(1)$ nm and $w = 0.36(5)$. (b) Atomic resolution image of two crystalline NPs. (c) Disordered Au clusters surrounded by Au single atoms.
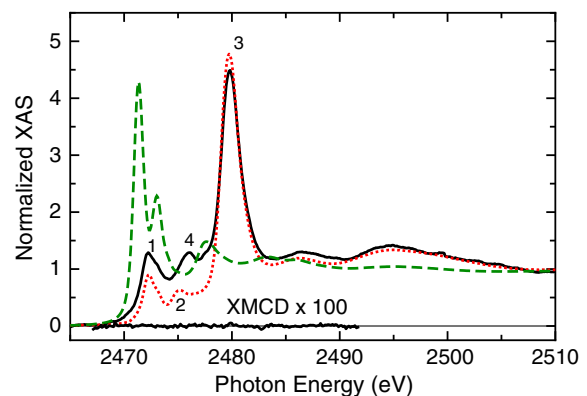

FIG. 2 (color online). XANES and XMCD spectra at the sulphur K edge of the S layer (dotted line), S layer with Au NPs (solid line), and L-cysteine (dashed line). Peaks 1 and 2 are due to S-layer cysteine, while peak 3 can be associated with sulfonyl groups. The S-Au resonance gives rise to a difference in intensity at 2476.1 eV (peak 4). The XMCD of the S layer containing Au NPs is shown at the bottom.
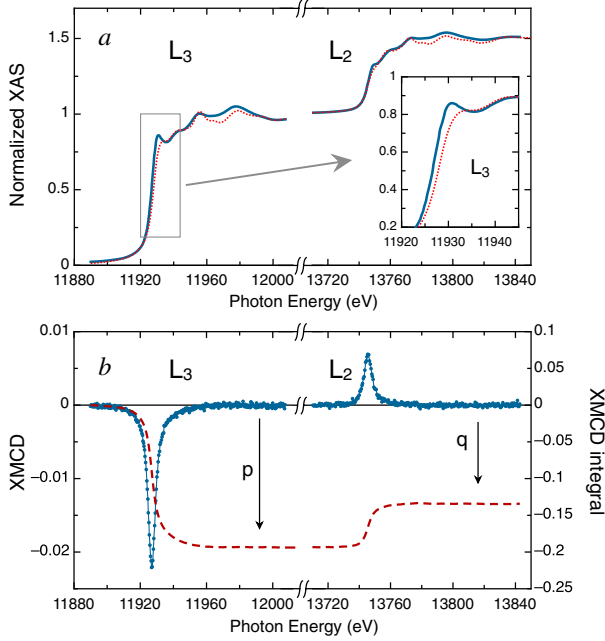
FIG. 3 (color online). (a) Comparison of $L_{2,3}$ Au XAS spectra measured on a metal Au foil (dashed line), and on Au NPs on S-layer ghosts (solid line). Inset: Details of the Au L_3 edge. (b) XMCD spectra at $T = 2.7$ K and $H = 170$ kOe (●). Integral of the XMCD signal (dashed line). The arrows indicate the high energy limits of the p and q integrals.

the orbital, spin, and total magnetic moments from the p and q integrals indicated in Fig. 3(b), as the dipolar term T_z is neglected in this case since the internal symmetry is cubic [21]. The resulting values $m_L = 0.0113(3)$ μ_B and $m_S = 0.0397(5)$ μ_B yield a net average magnetic moment per Au atom $m_{Au} = 0.051(1)$ μ_B/Au at $T = 2.7$ K and $H = 170$ kOe, and an orbital to spin ratio $m_L/m_S = 0.28(1)$.

Isothermal field-dependent XMCD data were recorded by changing the helicity of the beam, at the energy of the L_3 XMCD maximum at fixed photon energy ($E = 11927.9$ eV), while varying the field $-170 < H < +170$ kOe, at $T = 2.7$, 4.5 and 10 K, as shown in Fig. 4(a). The field dependence of the magnetization is well described by the classical Langevin function:

$$M(H) = m_{at}\left[\coth\left(\frac{M_{part}H}{k_BT}\right) - \frac{k_BT}{M_{part}H}\right], \quad (1)$$

where m_{at} is the average magnetic moment per Au atom, and M_{part} the mean magnetic moment per Au particle. The shape of the Langevin curve gives, therefore, information on the magnetic moment of each individual particle. The data are plotted in Fig. 4(a) as a function of $x = \frac{M_{part}H}{k_BT}$, with $M_{part} \sim 2.4(1)$ μ_B. The curves obtained at different temperatures fulfill a corresponding states law, showing the paramagnetic nature of the contribution from the Au $5d$ states. At $T = 2.7$ K and $H = 100$ kOe, the Pauli
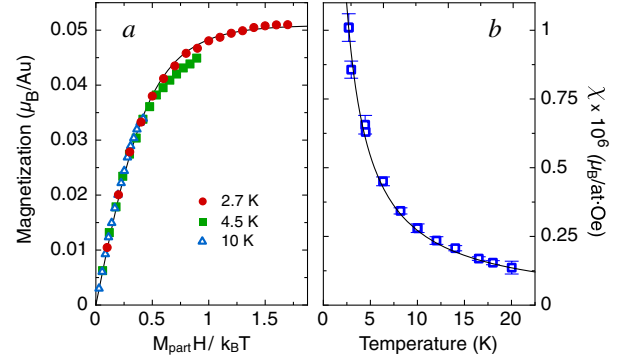

FIG. 4 (color online). (a) XMCD(x) curves measured at $T = 2.7$ (●), 4.5 (■) and 10 K (△) up to $H = 170$ kOe. They obey a corresponding state law and can be fitted by a Langevin function (solid line). (b) Magnetic susceptibility determined from XMCD(H) measurements at different temperatures (□). Curie's law for a collection of identical paramagnetic NPs (solid line).

paramagnetic contribution amounts to only about 4% of the total XMCD signal [12].

We also measured XMCD as a function of field in the range $-20 < H < 20$ kOe at several fixed temperatures between 2.7 and 20 K to determine the XMCD/H slope, i.e., the static susceptibility per Au atom $\chi_{at}(T)$ near $H = 0$. In Fig. 4(b), $\chi_{at}(T)$ is shown to follow Curie's law, $\chi_{at}(T) = C_{Curie}/T$, with $C_{Curie} = 2.78(5) \times 10^{-6}$ μ_B/atKOe^{-1}. The analysis of the magnetization and susceptibility data determined from the XMCD measurements is consistent with the existence of magnetic particles with 2.4–2.7 μ_B/particle. Besides, no XMCD signal was detected at the sulphur K edge (see Fig. 2).

Magnetization measurements have been performed with a commercial SQUID magnetometer with reciprocating sample option (RSO). Moreover, ac magnetic susceptibility, $\chi_{ac}(T)$, was measured at $T \geq 16$ mK and zero field, with a homemade microSQUID ac susceptometer installed inside the mixing chamber of a ^{3}He-^{4}He refrigerator [22].

The inset of Fig. 5(a) shows $M(H)$ data obtained at $T = 2.7$, 4.5, and 10 K up to $H = 50$ kOe, after subtracting a temperature independent diamagnetic contribution and a background contribution from the sample holder. The three $M(H)$ curves show a paramagnetic behavior and scale to a common Langevin function [Eq. (1)], with $M_{part} = 2.36(7)$ μ_B. The $M(H)$ and XMCD(H) nearly coincide. Figure 5(a) shows $M(H)$ data scaled to the average magnetization per Au atom, as deduced from the XMCD(H) measurements. These experiments show the presence of a paramagnetic magnetization which originated at the Au $5d$ band, with an average saturation moment per Au atom $m_{Au}^S = 0.055\mu_B$/Au.

In Fig. 5(b), the ac susceptibility of Au NPs on the S layer is shown. Data have been scaled with SQUID magnetization results at $T = 2.7$ K. We observe a frequency independent paramagnetic behavior without any indication for blocking of the Au magnetic moments.
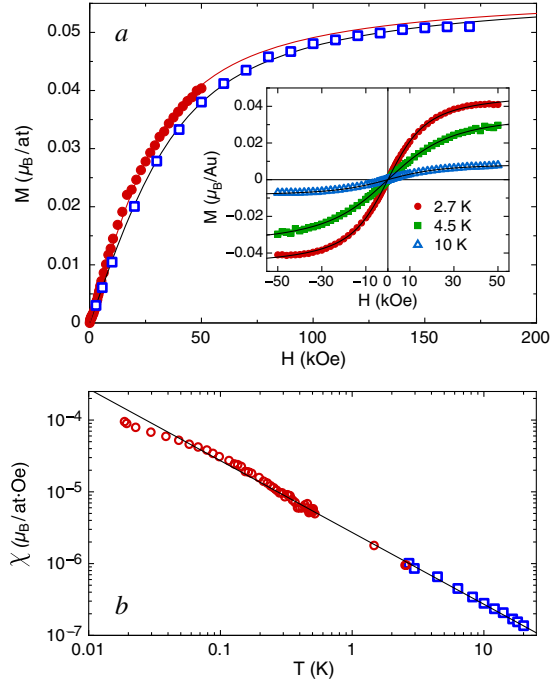
FIG. 5 (color online). Magnetization of Au NPs on a S layer.
(a) Comparison of $M(H)$ measured with SQUID ($\bullet$) with
XMCD(H) ($\square$) data at $T = 2.7$ K. The absolute values of the
magnetization are scaled using the XMCD(H) data. Inset: $M(H)$
data after subtraction of diamagnetic and background contributions, at $T = 2.7$ ($\bullet$), 4.5 ($\blacksquare$), and 10 K ($\triangle$). (b) Collected
magnetic susceptibility data: Susceptibility from XMCD(T) ($\square$)
measured at $H = \pm 20$ kOe, and ac susceptibility data as a
function of temperature ($\bigcirc$), scaled to the $T = 2.7$ K
XMCD(T) data. Curie's law fit (solid line).

From the analysis of the XMCD(H), XMCD(T), and
SQUID data one may conclude that there are Au nano-
particles with an average moment of $M_{part} = 2.4$ μ_B. The
number of atoms forming a particle with such a moment
and a homogeneous magnetization is $N_{part} = M_{part}/m_{Au} =$
44 atoms. These hypothetical NPs would have a diameter
of $\langle D \rangle = 1.1$ nm, with 6.7 transferred electrons to six
sulfur atoms to which the particle would be bound. In other
words, about one electron is taken up by each of the 6 S
atoms, which is quite reasonable.

Nanoparticles of $\langle D \rangle = 1.1$ nm have been detected by
TEM, as shown in the size distribution histogram, but they
are quite a minority. This fact allows us to suggest that not
all Au atoms in the sample are identical. For example, the
single Au atoms dispersed in the sample, and likely, some
of the clusters, because of the large size distribution, may
not be magnetic. Therefore, we conjecture that just an
unknown fraction f of the Au atoms are magnetic, and,
consequently the value of the magnetic Au atom would
increase as $m_{Au} = (0.055/f)\,\mu_B$.

The mechanism giving rise to the net moment per par-
ticle may be the spin-spin exchange coupling between
holes within each particle. The rather high and positive

$m_L/m_S = 0.28$ ratio is consistent with a rather high
spin-orbit coupling $\xi_{5d} = 608$ meV [23] and a more than
half-filled 5d band in Au. Therefore, the intra-atomic spin-
orbit coupling may also play a role in aligning the orbital
moment to the spins. The fact that we observe no blocking
down to 16 mK implies that the particle anisotropy is very
low, although a slight curvature in the ac susceptibility at
the lowest temperatures [Fig. 5(b)] could be indicative of
some degree of precursor of a spin blocking.

In recent studies [1,2] of Au NPs, paramagnetic (P) and
spontaneous (S) magnetization are recognized as general
features in most samples measured. For example, Au NPs
capped with dodecanethiol show a small S component,
usually persisting to high temperature, which yields a
minute XMCD Au $L_{2,3}$ signal (XMCD $\sim 10^{-5}$) [13],
although the authors propose a large moment per atom,
$m_{Au} = 0.33$ μ_B, by assigning the signal only to surface
atoms. Thiol-capped Au NPs embedded in polyethylene
[14] show also a very small ($< 10^{-4}$) XMCD signal as
compared to the ferromagnetic component. In Ref. [9], the
Curie type paramagnetism observed in the XMCD is
assigned to surface Au atoms, while the temperature
independent contribution is interpreted as due to the
Pauli paramagnetism of the core atoms. In contrast, our
XMCD signal is over 25 times larger than those found in
capped Au NPs.

In this work we only observe a P component; thus, the
observation of S and P components is very dependent on
the sample constitution. Moreover, such a large magnetic
moment fully rules out the possibility of a tiny amount of
magnetic impurity polarizing neighbor atoms as the source
of the observed Au magnetism. From experimental data
obtained on disordered AuFe alloys [24], one can estimate
that at least a 15% iron concentration would be needed to
generate a 5d magnetic moment of 0.05 μ_B per Au atom.
We performed XAS measurements at the Fe, Mn, Co, V
and Ni K edges that show no trace of magnetic impurities,
much less than a 15% percent level. This amount of
magnetic atoms, in turn, would yield a neat signal in
SQUID magnetometry, which we do not observe.

The XMCD signal we have measured is mostly associ-
ated to localized 5d orbitals. Therefore, recent models
proposed to explain the magnetism in Au as from orbital
origin, that consider quasifree electrons or holes [25,26]
from the 6sp conduction band, or unpairing of quantum-
confined conduction electrons excited thermally [27],
cannot explain our experimental results.

Our experimental results show, essentially, that on each
Au particle the thiols and other groups present in the
S-layer supply holes to the 5d band. Their spins are ferro-
magnetically coupled by a spin-spin exchange interactions.
In addition, an appreciable orbital moment is generated by
spin-orbit couplings. Hund's third rule is complied and
the orbital moment is parallel to the spins. The magnetic
behavior of the particle is paramagnetic, with very low

anisotropy. Thus, the external field sets the common alignment direction of the magnetization of all particles. The very large magnetic moment per Au atom observed in the XMCD measurements originates from the large charge transfer from the S layer supporting template to the Au surface atoms, and reshuffling of holes to the particle core.

Concluding, we have observed the largest magnetic moment per Au atom in NPs or any other configuration. The magnetic behavior is paramagnetic with very low anisotropy. The striking magnetic properties of these Au NPs are due to the special synthesis on a unique biological matrix containing low number of thiol groups distributed in a highly ordered way.

---

*barto@unizar.es

[1] J. de la Venta, E. F. Pinel, M. García, P. Crespo, A. Hernando, O. R. de la Fuente, A. Fernández, and S. Penadés, Mod. Phys. Lett. B **21**, 303 (2007).

[2] S. Trudel, Gold Bull. (London) **44**, 3 (2011).

[3] S. Dieluweit, D. Pum, and U. B. Sleytr, Supramol. Sci. **5**, 15 (1998).

[4] S. Selenska-Pobell, T. Reitz, R. Schonemann, T. Herrmannsdorfer, M. Marroun, A. Geissler, J. Bartolomé, F. Bartolomé, L. M. García, F. Wilhelm, and A. Rogalev, Nanomater. Nanotechnol. **1**, 8 (2011).

[5] J. Bartolomé, L. M. García, F. Bartolomé, F. Luis, R. López-Ruiz, F. Petroff, C. Deranlot, F. Wilhelm, A. Rogalev, P. Bencok, N. B. Brookes, L. Ruiz, and J. González-Calbet, Phys. Rev. B **77**, 184420 (2008).

[6] F. Wilhelm, M. Angelakeris, N. Jaouen, P. Poulopoulos, E. T. Papaioannou, C. Mueller, P. Fumagalli, A. Rogalev, and N. K. Flevaris, Phys. Rev. B **69**, 220404(R) (2004).

[7] F. Wilhelm, P. Poulopoulos, V. Kapaklis, J. P. Kappler, N. Jaouen, A. Rogalev, A. N. Yaresko, and C. Politis, Phys. Rev. B **77**, 224414 (2008).

[8] I. Carmeli, G. Leitus, R. Naaman, S. Reich, and Z. Vager, J. Chem. Phys. **118**, 10 372 (2003).

[9] Y. Yamamoto, T. Miura, M. Suzuki, N. Kawamura, H. Miyagawa, T. Nakamura, K. Kobayashi, T. Teranishi, and H. Hori, Phys. Rev. Lett. **93**, 116801 (2004).

[10] P. Crespo, R. Litrán, T. Rojas, M. Multigner, J. M. de la Fuente, J. C. Sánchez-López, M. A. García, A. Hernando, S. Penadés, and A. Fernández, Phys. Rev. Lett. **93**, 087204 (2004).

[11] C.-Y. Li, C.-M. Wu, S. K. Karna, C.-W. Wang, D. Hsu, C.-J. Wang, and W.-H. Li, Phys. Rev. B **83**, 174446 (2011).

[12] M. Suzuki, N. Kawamura, H. Miyagawa, J. S. Garitaonandia, Y. Yamamoto, and H. Hori, Phys. Rev. Lett. **108**, 047201 (2012).

[13] J. Garitaonaindia, M. Insausti, E. Goikolea, M. Suzuki, J. D. Cashion, N. Kawamura, H. Ohsawa, I. G. de Muro, K. Suzuki, F. Plazaola, and T. Rojo, Nano Lett. **8**, 661 (2008).

[14] J. de la Venta, V. Bouzas, A. Pucci, M. Laguna-Marco, D. Haskel, S. te Velthuis, A. Hoffmann, J. Lal, M. Bleuel, G. Ruggeri, C. de Julián-Fernández, and M. García, J. Nanosci. Nanotechnol. **9**, 6434 (2009).

[15] K. Taylor, J. Deatherage, and L. Amos, Nature (London) **299**, 840 (1982).

[16] E. Goikolea, J. S. Garitaonandia, M. Insausti, I. G. D. Muro, M. Suzuki, T. Uruga, H. Tanida, K. Suzuki, D. Ortega, F. Plazaola, and T. Rojo, J. Appl. Phys. **107**, 09E317 (2010).

[17] P. Zhang, A. Y.-C. Chu, T.-K. Sham, Y. Yao, and S.-T. Lee, Can. J. Chem. **87**, 335 (2009).

[18] Y. A. Perlov (private communication).

[19] A. Rogalev, F. Wilhelm, N. Jaouen, J. Goulon, and J.-P. Kappler, *X-ray Magnetic Circular Dichroism: Historical Perspective and Recent Highlights* (North-Holland, Amsterdam, 1999), Chap. 171, pp. 177–264.

[20] B. T. Thole, P. Carra, F. Sette, and G. van der Laan, Phys. Rev. Lett. **68**, 1943 (1992); P. Carra, B. T. Thole, M. Altarelli, and X. Wang, Phys. Rev. Lett. **70**, 694 (1993).

[21] R. Wu and A. J. Freeman, Phys. Rev. Lett. **73**, 1994 (1994).

[22] M. J. Martínez-Pérez, J. Sesé, F. Luis, D. Drung, and T. Schurig, Rev. Sci. Instrum. **81**, 016108 (2010).

[23] M. Vijayakumar and M. S. Gopinathan, J. Mol. Struct. **361**, 15 (1996).

[24] F. Wilhelm, P. Poulopoulos, V. Kapaklis, J. P. Kappler, N. Jaouen, A. Rogalev, A. N. Yaresko, and C. Politis, Phys. Rev. B **77**, 224414 (2008).

[25] A. Hernando, P. Crespo, and M. A. García, Phys. Rev. Lett. **96**, 057206 (2006).

[26] A. Hernando, P. Crespo, M. A. García, M. Coey, A. Ayuela, and P. M. Echenique, Phys. Status Solidi B **248**, 2352 (2011).

[27] C.-M. Wu, C.-Y. Li, Y.-T. Kuo, C.-W. Wang, S.-Y. Wu, and W.-H. Li, J. Nanopart. Res. **12**, 177 (2010).